Applied Catalysis B: Environmental 182 (2016) 587–597

Contents lists available at ScienceDirect

Applied Catalysis B: Environmental

journal homepage: www.elsevier.com/locate/apcatb

Solvent-free in situ synthesis of g-C_3N_4/{0 0 1}TiO_2 composite with enhanced UV- and visible-light photocatalytic activity for NO oxidation

Xu Song, Yun Hu*, Mengmeng Zheng, Chaohai Wei

Guangdong Provincial Key Laboratory of Atmospheric Environment and Pollution Control, The Key Lab of Pollution Control and Ecosystem Restoration in Industry Clusters, Ministry of Education, School of Environment and Energy, South China University of Technology, Guangzhou 510006, PR China

ARTICLE INFO

Article history:
Received 21 June 2015
Received in revised form 19 August 2015
Accepted 5 October 2015
Available online 14 October 2015

Keywords:
{0 0 1}TiO_2
g-C_3N_4
Composite
Photocatalytic oxidation
NO

ABSTRACT

Many possible applications of anatase TiO_2 nanosheets with exposed {0 0 1} facets ({0 0 1}TiO_2) are limited by its low quantum efficiency and no-spectral response in the visible region. We report on a simple solvent-free in situ method for synthesizing g-C_3N_4/{0 0 1}TiO_2 composite that over comes these drawbacks. The in situ growth of g-C_3N_4 and the removal of F^- ions on the {0 0 1}TiO_2 surface that remain from the synthesis process were simultaneously achieved during the calcination of a mixture of prepared {0 0 1}TiO_2 and urea, resulting in a compact connection between the two components, which facilitated the interfacial charge transfer process. The growth of g-C_3N_4 during the calcination process preserved the {0 0 1} facets of TiO_2. The composite samples exhibited higher photocatalytic activity than either the pure g-C_3N_4 or {0 0 1}TiO_2 nanosheets separately. Specifically, as measured by the removal of NO, the optimal composite sample, with a g-C_3N_4 content of 10%, was 2.4 times more effective than pure {0 0 1}TiO_2, 4.1 times more effective than g-C_3N_4 under UV light, and 5.8 times more effective than g-C_3N_4 under visible light irradiation. Also, the composite prepared by this method showed much higher activity than similar composites that were prepared by evaporation and mechanical methods. The new method is simple and holds the promise of expanded large-scale production and wider use of {0 0 1}TiO_2 based catalysts in the future.

1. Introduction

Since the discovery of photolysis of water at a TiO_2 electrode in 1972 [1], the researches and applications involving semiconductor photocatalysis have expanded into numerous fields, such as solar energy conversion [2], sensors [3], medication [4], thermocatalysis [5] and photocatalysis [6,7]. Among these uses, the applications related to environmental remediation have attracted much attention because of the growing concerns about the environment. In order to remediate the degraded environments, many new photocatalysts, other than TiO_2, have been developed; e.g., Bi-based [8–10], W-based [11,12] and In-based [13,14] compounds. However, TiO_2 is still one of the best photocatalysts for a number of reasons, including the fact that the redox potentials of its conduction band and valence band are favorable for hydroxyl radical production. Also, TiO_2 is relatively inexpensive, non-toxic, easily accessible, and stable against photolytic and chemical attack, in addition to exhibiting favorable photocatalytic activity [15–17].

Theoretical and experimental studies show that, in general, the anatase TiO_2 {0 0 1} facets are thermodynamically unstable and, hence, more reactive than the {1 0 1} facets which are the more common facets of anatase TiO_2 [18]. Both anatase TiO_2 sheets with {1 0 1} facets exposed ({1 0 1}TiO_2) and those with {0 0 1} facets exposed ({0 0 1}TiO_2) can only be excited by ultraviolet (UV) light due to the large band gap of 3.2 eV, a property that restricts the widespread use of anatase TiO_2 in many cases.

To address this problem, doping has been used to make {0 0 1}TiO_2 visible light responsive; e.g., N doping [19], C doping [20] and N-S co-doping [21]. Although these efforts have met with some success, it has not been easy to generate a visible light responsive {0 0 1}TiO_2 because the high crystallinity of the material makes it difficult to introduce the dopants into the bulk of the anatase TiO_2 sheets employing mild post-processing methods. It has also proven difficult to introduce the dopants during the growth of TiO_2 sheets themselves without disturbing the formation of the anatase TiO_2 {0 0 1} facets [17]. In addition, doping is strictly limited to a specific

* Corresponding author.
E-mail address: huyun@scut.edu.cn (Y. Hu).

http://dx.doi.org/10.1016/j.apcatb.2015.10.007
0926-3373/

concentration range because the excess dopants will act as new recombination centers and thereby reduce the quantum efficiency of catalyst, resulting in lower photocatalytic activity [22,23].

Noble metal deposition is a classical and often effective approach to making catalysts visible light responsive, including {0 0 1}TiO_2 [24,25]. However, the quest for more economically viable methods of visible light responsive catalysts goes on.

Other approaches to broadening the spectral response of a photocatalyst include coupling {0 0 1}TiO_2 with semiconductors that have a narrow band gap [26]. Moreover, suitable coupling between two semiconductors is beneficial for the interfacial charge transfer resulting in a higher quantum efficiency. In the present case, semiconductor coupling seems to be an ideal solution for {0 0 1}TiO_2 modification, because it not only overcomes the drawbacks of doping but also generates excellent photocatalytic activity, long-term stability and economical costing, but only if a suitable semiconductor can be found.

Carbon nitrides (C_3N_4), which have attracted much attention since their photocatalytic properties were discovered by Wang in 2009 [27], are a new type nonmetal semiconductor with outstanding mechanical, electrical, thermal, and optical properties [28]. C_3N_4 has been used as a narrow band gap semiconductor for coupling with other semiconductors, e.g., ZnO [29], CuTCPP [30] and TiO_2 [31]. However, reports about composite of graphitic-C_3N_4 (g-C_3N_4) and {0 0 1}TiO_2 (designated g-C_3N_4/{0 0 1}TiO_2) are few. Gu [32] obtained g-C_3N_4/{0 0 1}TiO_2 for the first time through a solvent evaporation method by mixing prepared g-C_3N_4 and {0 0 1}TiO_2 nanosheets in methanol for 12 h and then evaporating the mixture to dryness. Dai [33] synthesized a g-C_3N_4/{0 0 1}TiO_2 composite by adding prepared g-C_3N_4 to a Ti source before the hydrothermal process. In both studies, the g-C_3N_4 was used as a starting material to mix with {0 0 1}TiO_2 nanosheets or its precursor. In Gu's work, the contact between the g-C_3N_4 and {0 0 1}TiO_2 was established by a solid–solid post-processing method. However, the solid–solid contact between the two materials was less than optimal, which had a negative impact on both the catalytic activity and the long-term stability of the composite catalyst. In Dai's work, it was difficult to obtain TiO_2 with a high proportion of {0 0 1} facets because the presence of g-C_3N_4 in the hydrothermal process interfered with the TiO_2 crystal growth and probably obstructed the growth of {0 0 1} facets. Therefore, a better route of synthesis for the g-C_3N_4/{0 0 1}TiO_2 is needed.

In this paper, we report, for the first time to our knowledge, on a simple solvent-free in situ method for preparing composite of g-C_3N_4/{0 0 1}TiO_2 nanosheets using as-prepared {0 0 1}TiO_2 nanosheets as a starting material. The in situ growth of g-C_3N_4 on {0 0 1}TiO_2 and the simultaneous removal of F^- ions from the {0 0 1}TiO_2 surface was achieved by calcination of a mixture of {0 0 1}TiO_2 and urea, which was the precursor of g-C_3N_4. The composite catalyst showed enhanced photocatalytic activity beyond that of either pure {0 0 1}TiO_2 or g-C_3N_4, as demonstrating by the oxidation of NO under UV and visible light irradiation. Details of the synthesis and photocatalytic mechanism are provided and show the promise of this approach for further development and application to treatment of gaseous pollutants.

2. Experimental

2.1. Preparation of catalysts

All chemicals for synthesis were analytical grade and were used without further purification. Pure g-C_3N_4 was prepared by thermal polycondensation of urea (Fuchen, Tianjing). In a typical synthesis, 5 g of urea was placed in a semiclosed crucible with a cover and calcined at 550 °C for 2 h in air atmosphere using a heating rate of 15 °C min^{-1}. After being naturally cooled to room temperature, pale yellow g-C_3N_4 was obtained.

Pure {0 0 1}TiO_2 nanosheets were synthesized by a hydrothermal method. Typically, 4.4 mL of hydrofluoric acid (with a concentration of 40 wt%, Fuyu, Tianjing) was added into 20 mL of titanium tetrabutoxide (Sinoparm, Shanghai) with magnetic stirring for 30 min in a Teflon-lined autoclave, and then kept at 180 °C for 20 h. The resulting white precipitate was washed with ethanol (Sinoparm, Shanghai) and distilled water several times until the filtrate was neutral. The residual solid was dried in an oven at 100 °C for 8 h and then ground into fine powder, which consisted of {0 0 1}TiO_2 nanosheets with residual F^- ion on its surface and denoted as {0 0 1}TiO_2 (F). Generally, the F^- ions on the TiO_2 surface are not favorable for photocatalysis and should be removed before catalytic applications [34,35]. Our photocatalytic experiment results shown in Fig. S1 and S2 also support this conclusion. Here, {0 0 1}TiO_2 (F) was calcined at 550 °C for 2 h in air atmosphere with a heating rate of 15 °C min^{-1} to remove the residual F^- ions, resulting in pure {0 0 1}TiO_2.

The synthesis of g-C_3N_4/{0 0 1}TiO_2 composite is quite simple. A certain amount of aforementioned {0 0 1}TiO_2(F) and 5 g of urea were mixed in a crucible. Then, the mixture in a semiclosed crucible was heated to 550 °C at a heating rate of 15 °C min^{-1} and maintained for 2 h. In the calcination process, the in situ growth of g-C_3N_4 on {0 0 1}TiO_2 and the removal of F^- on the {0 0 1}TiO_2 surface were simultaneously achieved. After cooling to room temperature, the g-C_3N_4/{0 0 1}TiO_2 composite was obtained. The prepared samples were denoted as CT-*x*, where *x* is the weight percentage of g-C_3N_4 in the whole sample. For comparison, a mechanical mixture of g-C_3N_4 and {0 0 1}TiO_2 as well as a sample via a solvent evaporation method [32] were also prepared with 10 wt% of g-C_3N_4 and were denoted as Mech-10 and Evap-10, respectively. Briefly, Evap-10 was prepared by mixing of the prepared 20 mg of g-C_3N_4 and 180 mg of pure {0 0 1}TiO_2 in 50 mL of methanol, then sonicated for 30 min, stirred in fume hood for 12 h until dryness and dried at 100 °C for 4 h.

2.2. Preparation of photoelectrode

The photoelectrode was prepared by the following process. 15 mm × 10 mm indium-tin oxide (ITO) glass was used in the present study. One edge of the ITO glass was carefully covered with insulating tape, leaving a 10 mm × 10 mm exposed conductive side of the ITO glass. 20 mg of the photocatalyst was dispersed in a mixed solution of 1 mL of ethanol and 10 μL of naphthol to make a homogeneous suspension, in which the exposed area of the ITO glass dip-coated. After drying in an oven at 80 °C for 10 h, the insulating tape on ITO glass was removed.

2.3. Characterization of the composite

Powder X-ray diffraction (XRD) patterns were recorded with a D8 Advance diffractometer (Bruker AXS, Germany) with Cu Kα radiation (λ = 1.5418 Å). Fourier transform-infrared (FT-IR) was carried out on a Nicolet 6700 Fourier Transform IR spectrometer (Thermo, USA). Elemental analyses were performed on a Vario EL Cube elemental analyzer (Elementar, Germany). Scanning electron microscopy (SEM) was obtained using a Nova Nano SEM 430 field emission scanning electron microscope (FEI, USA). High-resolution transmission electron microscopy (HRTEM) analyses were conducted using a JEM-2100F electron microscope (JEOL, Japan) at an accelerating voltage of 200 kV. The electron microscopy samples were prepared by dispersing the powder in ethanol with ultrasonication for 30 min. Carbon-coated copper grids were used as sample holder. The UV–vis diffuse reflectance spectra (DRS) of the

samples over a range of 250–800 nm were recorded by a UV-2550 powder UV–vis spectrophotometer (Shimadzu, Japan) with a $BaSO_4$ reference. X-ray photoelectron spectroscopy (XPS) was performed on a Thermo Escalab 250Xi spectrometer (Thermo, USA) with a monochromatic Al Kα source. All the binding energies were referenced to the C1s peak at 284.8 eV of the surface adventitious carbon. Photoluminescence spectra (PL) were recorded using a Cary Eclipse Fluorescence spectrophotometer (Varian, Australia) under 324 nm excitation.

2.4. Photoelectrochemical measurements

Photocurrent measurements were conducted using a CHI 660B electrochemical analyzer (Chenhua, China) using a standard three-electrode system with a working electrode (photoelectrode), a platinum counter electrode and a Ag/AgCl reference electrode. A 300 W Xe lamp (PLS-SXE300, Perfect Light, China) with a UV cut off filter was used as visible light source, and a 125 W high pressure mercury lamp (Philips) was used as UV light source. 0.1 M Na_2S and 0.02 M Na_2SO_3 mixed aqueous solution was used as the electrolyte [36]. The i–t curves were measured at 0 V bias potential.

2.5. Evaluation of photocatalytic activity

The photocatalytic oxidation of NO was performed at ambient temperature in a continuous flow reactor. The experimental setup was described in our previous work [37]. Briefly, a quartz rectangular reactor with inner volume of 4.5 mL (60 mm × 15 mm × 5 mm) was used as the photoreactor for the photocatalytic oxidation of NO. A 125 W high pressure mercury lamp (Philips) was used for UV light source, while a 500 W commercial tungsten halogen lamp (General Electric) with a glass filter that cut off the light below 420 nm was used for visible light source. The light intensities were 1.6 mW cm^{-2} (UV at 365 nm) and 0.7 mW cm^{-2} (Vis at 420 nm), respectively, measured with a UVA radiometer (Photoelectric Instrument Factory of Beijing Normal University). Two fans were fixed around the lamp to prevent a rise in temperature in the flow system. The amount of catalyst for each experiment was kept at 20 mg. The feed gas of ca. 40 ppm NO with the flow rate of 200 mL min^{-1} and humidity of 70% was obtained by diluting NO in a compressed gas cylinder with a concentration of 1000 ppm with N_2 and wet air stream. The concentration of NO was continuously measured at the outlet of the reaction system by an NO analyzer equipped an infrared spectrum detector (GXH-1050E, Beijing Junfang Co., Ltd.). After 10 min in the dark when the NO adsorption-desorption equilibrium was achieved, the lamp was turned on. Reference experiments were conducted and the results showed that NO could not be eliminated when the reactor was illuminated in the absence of a photocatalyst or in the presence of the photocatalyst without illumination.

In the data analysis, the NO conversion was defined as the removal rate of NO at some time point. In addition, in order to determine how much NO could be removed by the photocatalysis within the continuous flow photoreactor, we integrated the variation of NO instantaneous concentration over time. The integral was denoted as NO removal, in which the contribution by the 10 min adsorption in dark was not included. Computational formulas are shown below:

$$\text{NO conversion}\ (\%) = \frac{NO_{in} - NO_{out}}{NO_{in}} \times 100\%$$

$$\text{NO removal}\ (\mu\text{mol} \times 20\text{mg}^{-1}) = \int \frac{f}{22.4} \times (NO_{in} - NO_{out})dt$$

where f was the quantity of reaction air flow under standard state.

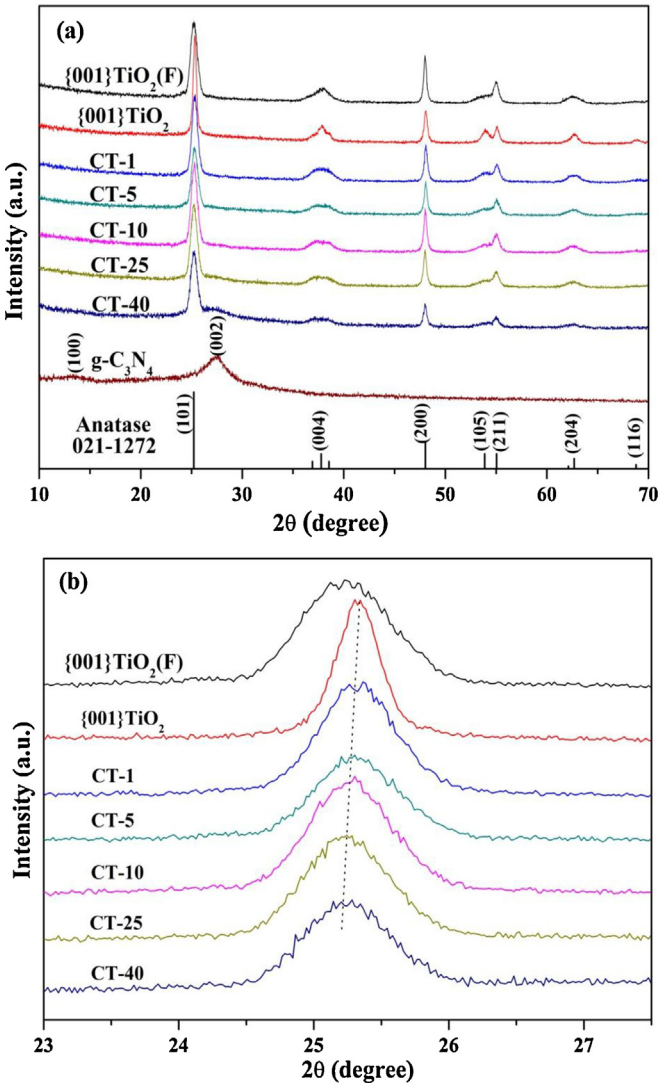

Fig. 1. (a) XRD patterns of {0 0 1}TiO_2(F), {0 0 1}TiO_2, g-C_3N_4 and CT-x (x = 1%, 5%, 10%, 25%, 40%). (b) The (1 0 1) diffraction peak of {0 0 1}TiO_2(F), {0 0 1}TiO_2 and CT-x (x = 1%, 5%, 10%, 25%, 40%).

3. Results and discussion

3.1. XRD and FT-IR analyses

The phase and crystallite structure of g-C_3N_4, {0 0 1}TiO_2 and their composites were investigated by XRD analyses. As shown in Fig. 1a, all diffraction peaks of {0 0 1}TiO_2(F) and {0 0 1}TiO_2 can be indexed to the anatase TiO_2 (JCPDS 021-1272), indicating that the anatase phase was completely preserved after calcination at 550 °C. However, closed examination showed that the full-width at half maximum (FWHM) of the (0 0 4) peak was reduced at the same time that the intensities of (1 0 1) and (1 0 5) diffraction peaks became stronger as a result of calcination. This finding indicates that the anisotropic growth of TiO_2 sheet along c-axis was debilitated and (0 0 1) surface began to convert into thermodynamic stable (1 0 1) facets via (1 0 5) facets during the heat treatment [38]. Obviously, the (0 0 4) FWHM of CT-x was wider than that of {0 0 1}TiO_2, which implied that the formation of g-C_3N_4 during calcination process favored the preservation of (0 0 1) facets. In addition, from CT-1 to CT-40, the peak intensities ascribed to anatase TiO_2 gradually diminished, which may be attributed to the increased g-C_3N_4 concentration in the composites. Two evident

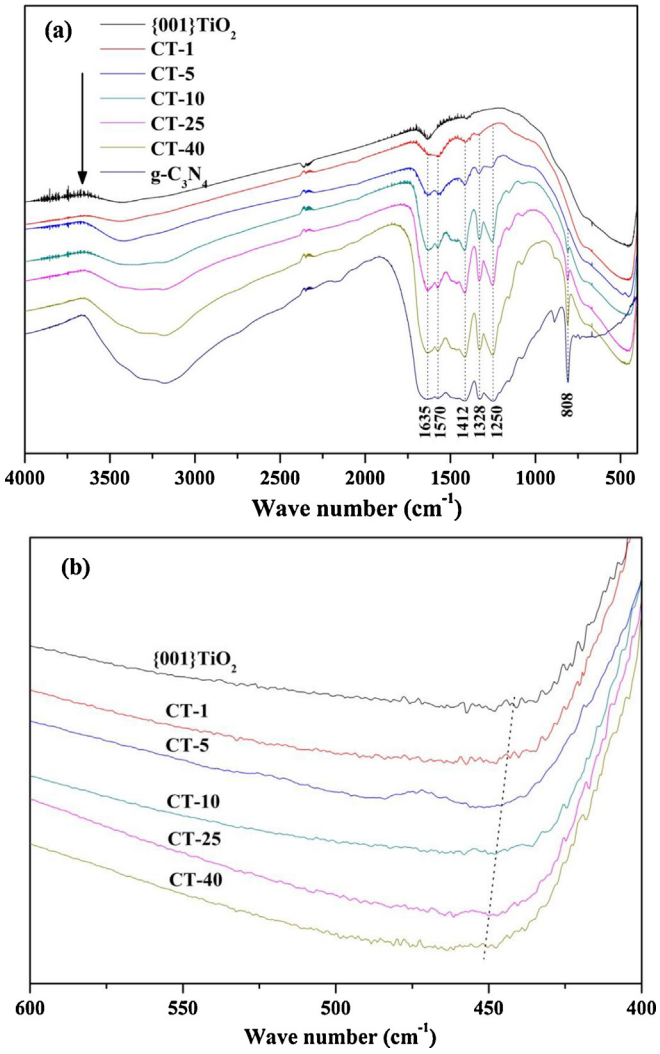

Fig. 2. FT-IR spectra of {0 0 1}TiO_2, g-C_3N_4 and CT-*x* (*x* = 1%, 5%, 10%, 25%, 40%).

peaks of g-C_3N_4 appearing at 13.1° and 27.4° correspond to the (0 0 2) and (1 0 0) planes, which can be indexed to the characteristic in-planar structural packing and inter-planar stacking peaks of the aromatic systems in graphite-like carbon nitride, respectively [39]. For all CT-*x*, only CT-40 shows distinct (0 0 2) diffraction peak of g-C_3N_4, which may be a result of the low content or uniform distribution of g-C_3N_4. In Fig. 1b, the (1 0 1) diffraction peak of {0 0 1}TiO_2(F) moved to the bigger diffraction angle after be calcined into {0 0 1}TiO_2, but then it moved slightly to the smaller diffraction angle after coupling with g-C_3N_4, which implies that the formation of g-C_3N_4 favors preservation of the crystal structure of {0 0 1}TiO_2(F) in the calcination process.

Fig. 2a shows the FT-IR spectra of g-C_3N_4, {0 0 1}TiO_2, and their composites. For pure g-C_3N_4, characteristic absorption bands within 1200–1670 cm^{-1} region and at 808 cm^{-1} are shown in the spectrum. Specifically, the absorption bands at 1250, 1328, 1412 and 1570 cm^{-1} were attributed to aromatic C—N stretching, and the band at 1635 cm^{-1} was attributed to C—N stretching, while the absorption band at 808 cm^{-1} was assigned to out of plane skeletal bending modes of the triazine cycles [40,41]. The broad absorption band within 3000–3600 cm^{-1} was attributed to N—H stretching vibration of residual NH (or NH_2) group attached to the sp^2 hybridized carbon or O—H stretching associated with adsorbed water [42,43]. For pure {0 0 1}TiO_2, the characteristic absorption band attributed to Ti—O—Ti stretching emerged at 447 cm^{-1} [44]. In addition, the absorption band at 1630 cm^{-1} and around 3400 cm^{-1} was assigned to surface —OH stretching or adsorbed water. In the case of CT-*x* composites, both characteristic absorption bands of g-C_3N_4 and {0 0 1}TiO_2 could be observed in the spectra.

Along with the increase of the C_3N_4 content, relative intensities of characteristic bands representing g-C_3N_4 in the spectra increased. Furthermore, from the narrow scan spectra (Fig. 2b), it can be found that the Ti—O—Ti stretching was slightly shifted towards to higher wave number along with the increase of the g-C_3N_4 content. This may be interpreted that the chemical environment of {0 0 1}TiO_2 surface was changed after combined with g-C_3N_4. It is known that when the connect between g-C_3N_4 and {0 0 1}TiO_2 becomes very close, the molecular orbitals of them may interact. Thus, for {0 0 1}TiO_2, its chemical environment would changed after compositing with g-C_3N_4. So, it can be deduced reversely that a tight contact at the interface between g-C_3N_4 and {0 0 1} TiO_2 has been achieved.

Table 1
Elemental analysis results of {0 0 1}TiO_2, g-C_3N_4 and CT-*x* (*x* = 1%, 5%, 10%, 25%, 40%).

Sample	N%	C%	H%	C/N molar ratio	C_3N_4 wt% (without H)
{0 0 1}TiO_2	0	0.22	0.347		0
{0 0 1}TiO_2	0	0.05	0.148		0
g-C_3N_4	60.40	33.98	1.956	0.656	0
CT-1	0.66	0.40	0.297	0.707	1.06
CT-5	3.40	2.00	0.239	0.686	5.40
CT-10	6.18	3.55	0.334	0.670	9.73
CT-25	16.57	9.43	0.684	0.664	26.00
CT-40	25.53	14.43	1.039	0.659	39.96

3.2. Elemental analyses

Elemental analysis results are listed in Table 1. For pure g-C_3N_4, the C/N atomic ratio 0.656 was lower than the theoretical C/N ratio of 0.75, which may be attributed to the presence of uncondensed amino groups generated in the calcination process [45]. In addition, the presence of amino groups observed by FT-IR analyses confirmed this conclusion. All composite samples presented higher C/N ratios than pure g-C_3N_4, which implies that the presence of {0 0 1}TiO_2 was favored in the formation process of g-C_3N_4. Zou's Work [46] also showed that Ti—OH can significantly facilitate the polymerization of g-C_3N_4. The g-C_3N_4 contents were calculated by summing up the C and N contents of each sample; the results were in accordance with the theoretical values.

3.3. Morphology

SEM and TEM analyses were used to investigate the morphology of g-C_3N_4, {0 0 1}TiO_2, and their composite. As Fig. 3a and Fig. S3b show, {0 0 1}TiO_2 were composed of thin TiO_2 nanosheets with 50–100 nm in side length, which is more obvious in the TEM image of {0 0 1}TiO_2 (Fig. S3d). Fig. 3b shows the SEM image of g-C_3N_4, which exhibits a wrinkled structure, which is more obvious in the TEM image of g-C_3N_4 (Fig. 3e). Fig. 3c and d show the SEM images of CT-10; all of the samples exhibited a uniform irregular fringe of flakes that were with 200 nm-1 μm in length and ca. 20 nm in thickness. The insert picture in Fig. 3d is the magnified image of a part of a single flake, in which single TiO_2 nanosheets are well-organized on a big board. The ordered arrangement of {0 0 1}TiO_2 was favorable for the effective contact with g-C_3N_4 and the improvement of catalytic activity. Fig. 3f is the TEM image of CT-10, in which TiO_2 nanosheets can be clearly observed in the sample edge, and a duller and thicker area caused by g-C_3N_4 can be observed within the image, too. Fig. 3g shows a HR-TEM images of the joint area between g-C_3N_4 and {0 0 1}TiO_2 in CT-10. The lattice spacing shown in Fig. 3g is ca. 0.35 nm, corresponding to the {1 0 1} planes of anatase TiO_2.

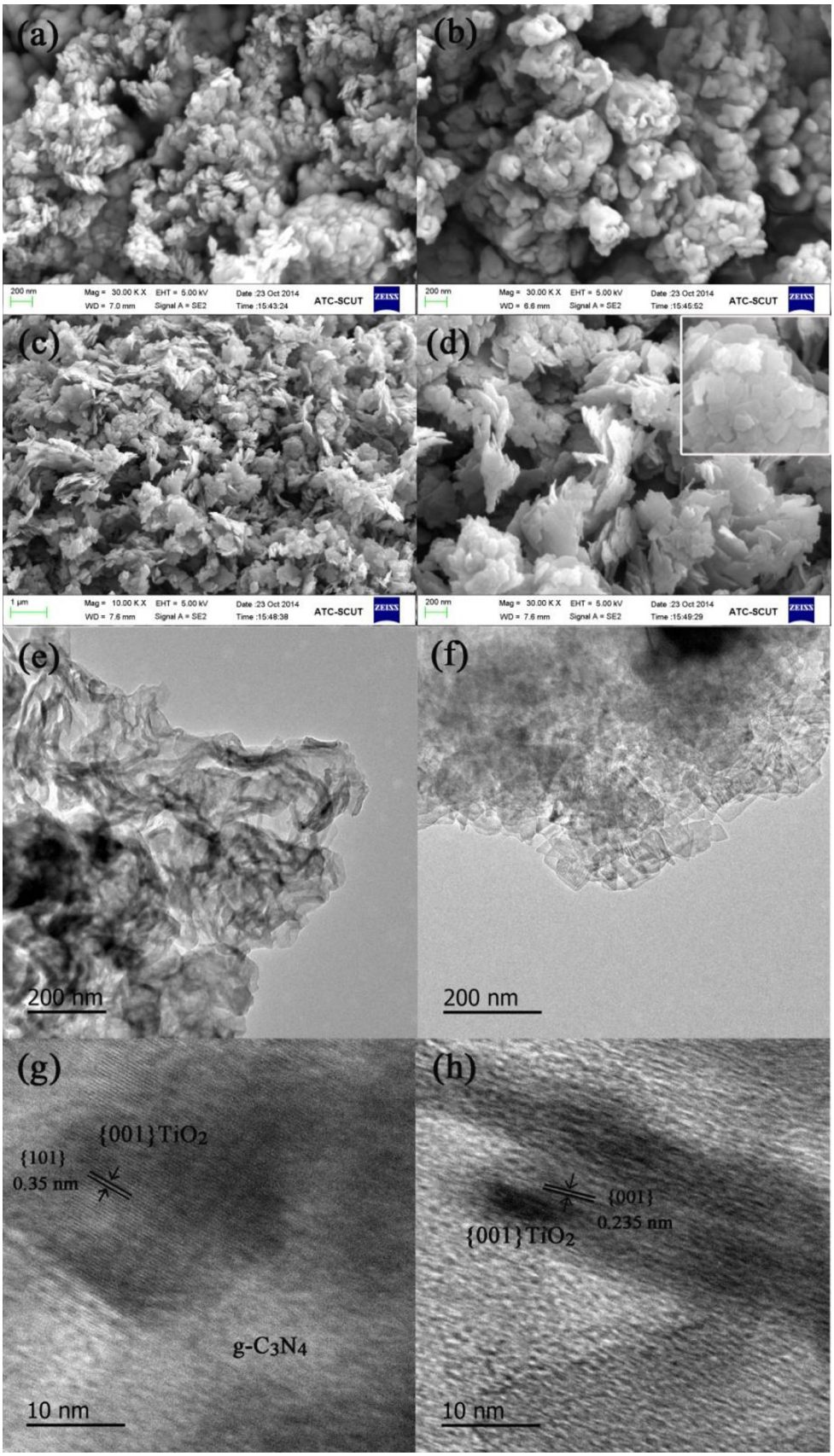

Fig. 3. SEM and TEM images of {0 0 1}TiO_2, g-C_3N_4 and CT-10. (a) SEM image of {0 0 1}TiO_2, (b) SEM image of g-C_3N_4, (c)(d) SEM images of CT-10, (e) TEM image of g-C_3N_4, (f–h) TEM images of CT-10.

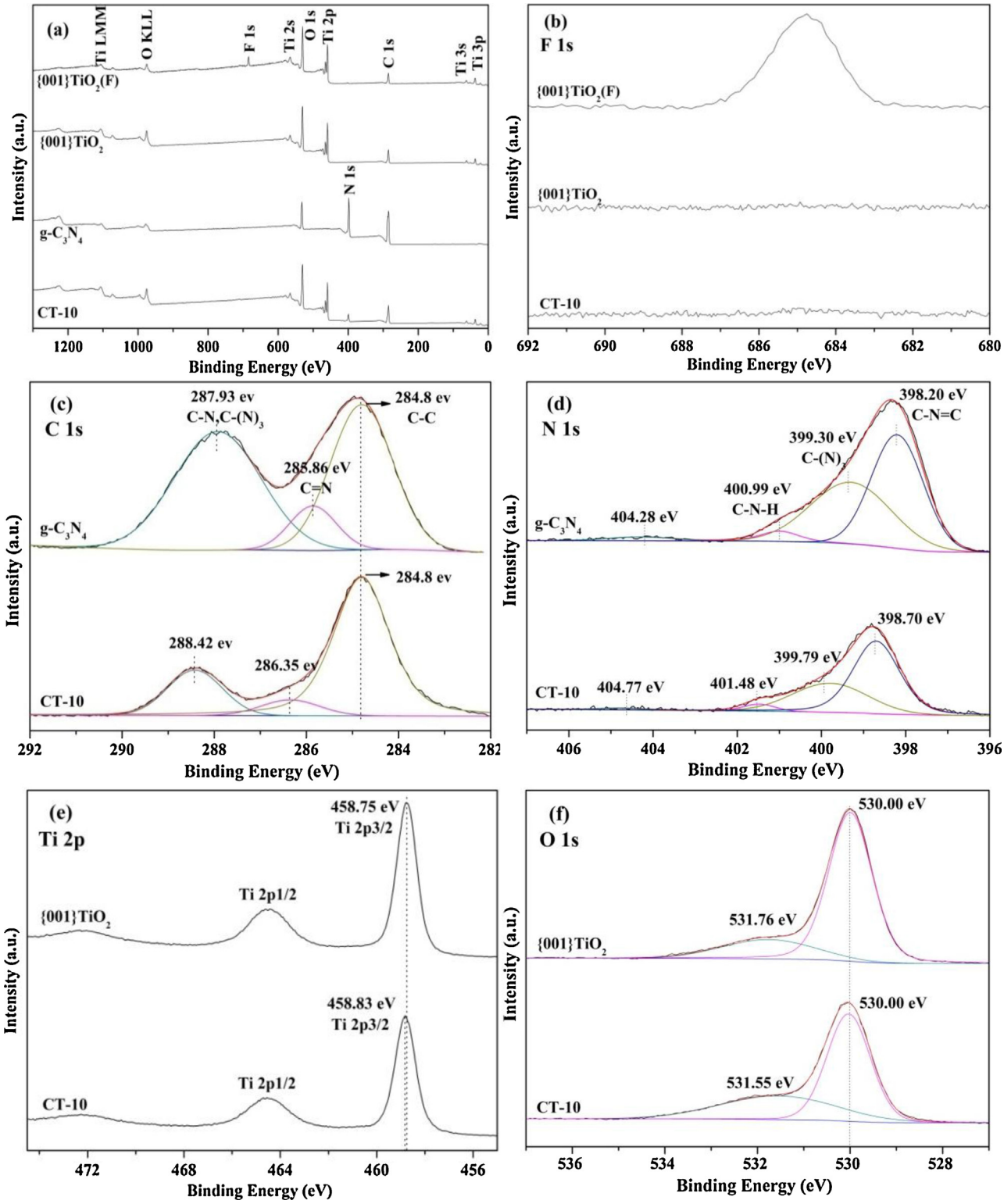

Fig. 4. Survey and high-resolution XPS spectra of samples. (a) Survey spectra; (b) F 1s spectra of {0 0 1} TiO_2 (F), {0 0 1}TiO_2 and CT-10; (c) C 1s spectra, (d) N 1s spectra of g-C_3N_4 and CT-10; (e) Ti 2p spectra, (f) O 1s spectra of {0 0 1}TiO_2 and CT-10.

This indicates that the flat top surfaces of {0 0 1}TiO_2 is {0 0 1} facets [17,32], and the coupling with g-C_3N_4 happened on the {0 0 1} facets of {0 0 1}TiO_2. This conclusion was confirmed by the side view HR-TEM images of CT-10 in Fig. 3h. The lattice spacing parallel to the top and bottom is ca. 0.235 nm, indicating that the flat top and bottom facets are exposed {0 0 1} facets [21].

3.4. XPS analysis

Both survey and high resolution XPS spectra were obtained. Fig. 4a shows the survey spectra of {0 0 1}TiO_2(F), {0 0 1}TiO_2, g-C_3N_4 and CT-10. The C 1s peak observed in spectrum of {0 0 1}TiO_2 is due to the surface adventitious carbon and the O 1s peak in the g-C_3N_4 spectrum is assigned to the adsorbed H_2O and O_2 on the

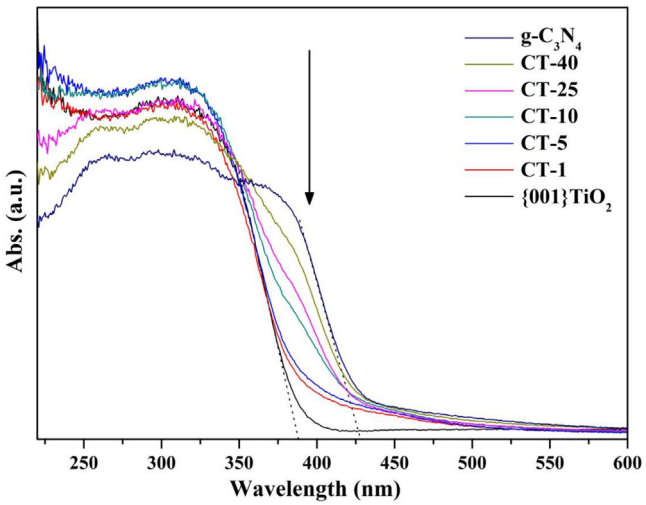

Fig. 5. UV–vis absorption spectra of {0 0 1}TiO_2, g-C_3N_4 and CT-*x* (*x* = 1%, 5%, 10%, 25%, 40%).

sample surface [47]. An F 1s peak was observed neither in the survey spectra (Fig. 4a) nor in the high-resolution F 1s spectra (Fig. 4b) of {0 0 1}TiO_2 and CT-10, indicating that residual F^- on {0 0 1}TiO_2 surface was removed by the calcination process.

The results of the high-resolution XPS spectra of C 1s, N 1s, Ti 2p and O 1s of the three samples are shown in Fig. 4c–f. Three peaks were obtained after deconvolution in the high-resolution XPS spectrum of C 1s for g-C_3N_4 (Fig. 4c). The peak at ca. 284.8 eV was assigned to the adventitious carbon; the peak at ca. 285.86 eV was assigned to the C=N groups; and the peak at ca. 287.93 eV was attributed to C—N or C-$(N)_3$ groups [48]. The C 1s spectrum for CT-10 was similar to that of g-C_3N_4, but the peaks of C=N and C—N (or C-$(N)_3$) shifted 0.49 eV towards higher binding energy. In the N 1s spectrum of g-C_3N_4 (Fig. 4d), four peaks can be observed after deconvolution. Peaks at ca. 398.16, 399.34, 400.85 and 404.25 eV could be assigned to sp^2-hybridized aromatic N (C=N—C), tertiary nitrogen N-$(C)_3$, C—N—H groups and charging effects, respectively [39,49,50]. Correspondingly, in the N 1s spectrum of CT-10, those four peaks shifted ca. 0.49 eV towards higher binding energy. The shifts of the C 1s and N 1s peaks of CT-10 could be attributed to the chemical environment change arising from the close interaction between g-C_3N_4 and {0 0 1}TiO_2 [47], which is consistent with the results of FT-IR and TEM measurements. As can be seen in Fig. 4e and f, the peak positions of Ti 2p and O 1s shifted slightly after {0 0 1}TiO_2 combined with g-C_3N_4.

3.5. UV–vis absorption spectra

Fig. 5 shows UV–vis absorption spectra of pure and composite samples, which were obtained from the UV–vis diffuse reflection spectra (DRS) through the Kubelka–Munk conversion. For pure {0 0 1}TiO_2, a significant absorption edge at ca.390 nm was assigned to the intrinsic anatase {0 0 1}TiO_2 band gap of 3.18 eV [20]. Niu et al. [51] reported that the band gap energy of g-C_3N_4 could shift from 2.77 to 2.97 eV when bulk g-C_3N_4 turned into g-C_3N_4 nanosheets. As shown in Fig. 5, the absorption edge of pure g-C_3N_4

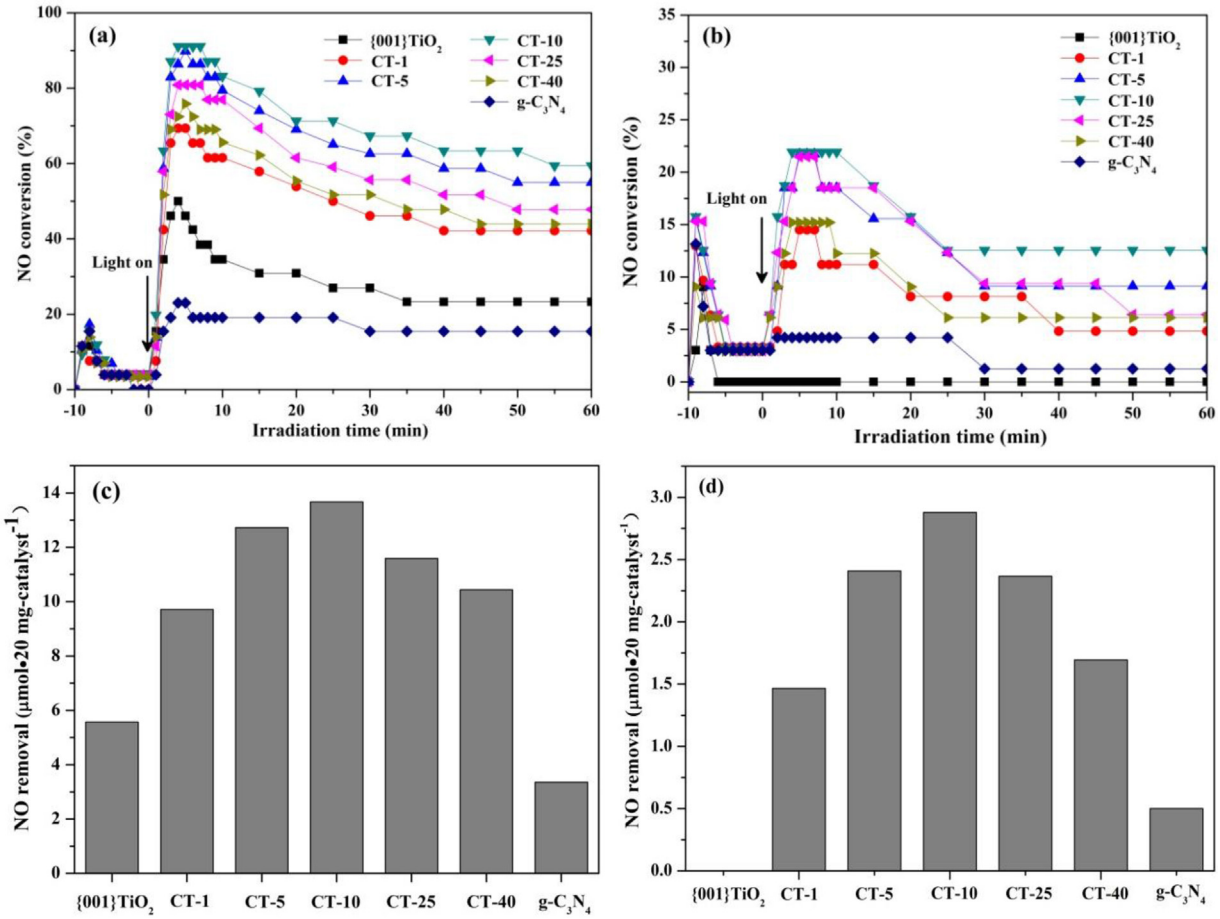

Fig. 6. NO conversion on {0 0 1}TiO_2, g-C_3N_4 and CT-*x* (*x* = 1%, 5%, 10%, 25%, 40%) over time under (a) UV light and (b) visible light irradiation. The total NO removal within 60 min of photoreaction over {0 0 1}TiO_2, g-C_3N_4 and CT-*x* for 20 mg catalyst under (c) UV light and (d) visible light irradiation.

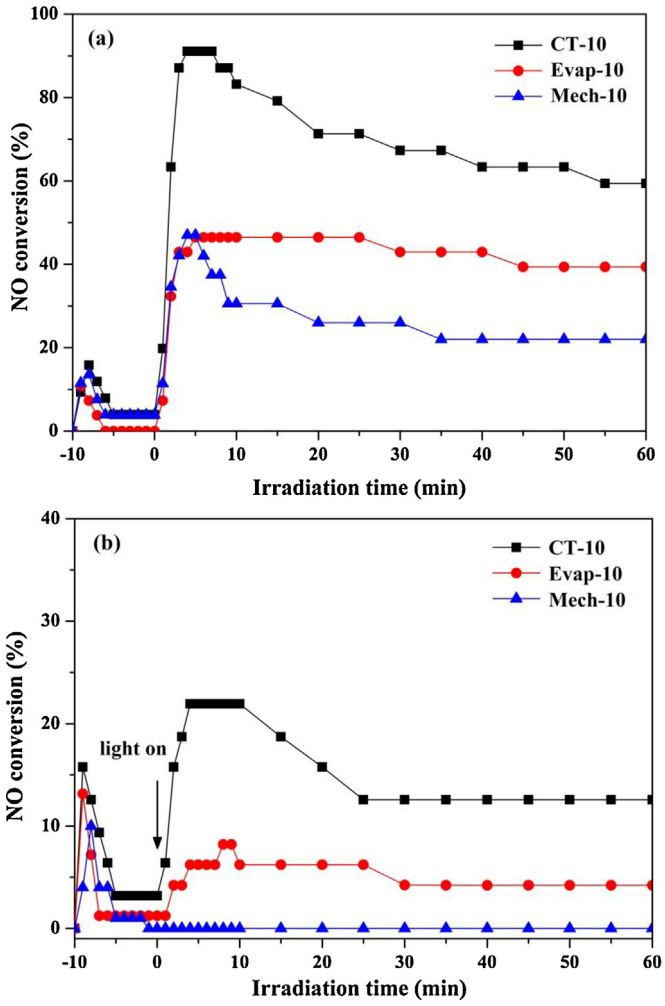

Fig. 7. NO conversion on CT-10, Mech-10 and Evap-10 under (a) UV light and (b) visible light irradiation.

is at ca. 430 nm, and the corresponding band gap energy is 2.88 eV, which is consistent with Niu's report. For the composite samples, the absorption intensities in UV region first increased and then decreased as the g-C_3N_4 content increased. In visible light region, the absorption edge of the composite samples showed an increasing red shift as the g-C_3N_4 content increased. For CT-1, although the trace amount of g-C_3N_4 did not result in an significant red shift of absorption edge, the light absorption from 370 to 500 nm was more efficient in comparison with pure {0 0 1}TiO_2.

3.6. Photocatalytic activity and stability

The photocatalytic activities of g-C_3N_4/{001}TiO_2 composites were evaluated through photo-oxidation of NO gas under UV and visible light irradiation, respectively. Figs. S4 and S5 show the instantaneous NO concentrations variations versus time in the presence of different samples under UV and visible light, respectively. The sag curves in the first 10 min before the illumination were caused by the NO adsorption/desorption process on the catalyst surfaces. When the light was turned on, for all samples, NO concentrations decreased rapidly and reached their minimum after exposure for 5 min. Then, NO concentrations increased gradually over time and reached a steady state concentration. These data were used to calculate NO conversion for the different samples, and the results are shown in Fig. 6a and b. Under UV light, after all samples reached their steady state at 60 min. CT-1, CT-5, CT-10, CT-25,

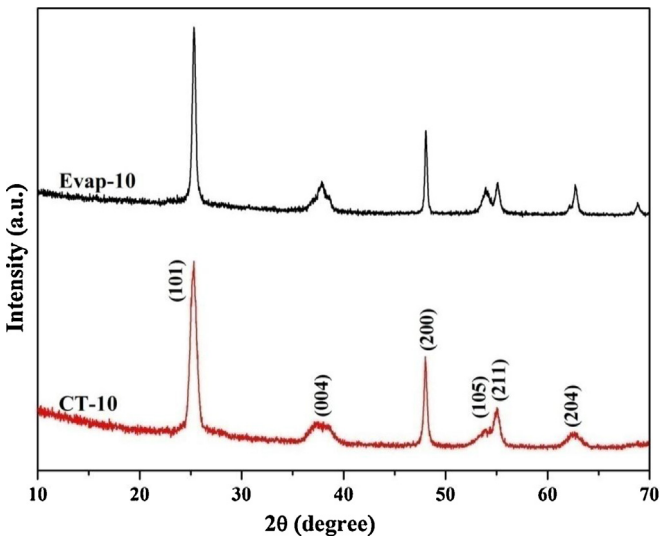

Fig. 8. XRD patterns of Evap-10 and CT-10.

CT-40 removed 42.2%, 55.0%, 59.4%, 47.8% and 43.9% of NO in the airflow, respectively, whereas only 23.3% of NO was removed by pure {0 0 1}TiO_2 and only 15.4% by g-C_3N_4. In contrast, under visible light the NO conversion for CT-1, CT-5, CT-10, CT-25, CT-40 at 60 min was 4.8%, 9.1%, 12.6%, 6.4% and 6.1%, respectively, which was much higher than that of pure g-C_3N_4 (1.2%). The significant improvement of NO conversion shows that the combination of {0 0 1}TiO_2 with g-C_3N_4, even with only 1 wt% of g-C_3N_4, can significantly enhance the photocatalytic activity of {0 0 1}TiO_2. Obviously, the performance of the composite samples was dependent on the ratio of g-C_3N_4 and {0 0 1}TiO_2. As the g-C_3N_4 content increased from 1 to 40 wt%, the NO conversion initially increased and then decreased, reaching a maximum at 10 wt% g-C_3N_4 content.

In order to evaluate the overall NO removal on the samples, the total NO removal within 60 min of photoreaction, the variation of instantaneous NO concentration was integrated over time. The results are shown in Fig. 6c and d. The amount of NO removed in 60 min with 20 mg of CT-10 catalyst exposed to UV and visible light was 13.7 and 2.9 μmol, respectively. These results are 2.4 and 4.1 times greater than that observed with UV light using pure {0 0 1}TiO_2 and g-C_3N_4, respectively (Fig. 6c), and 5.8 times greater than that observed with visible light using g-C_3N_4 (Fig. 6d).

In order to emphasize the importance of intimate coupling for the composite catalysts, the performance of three catalysts; i.e., CT-10, Mech-10 and Evap-10, were compared under both UV and visible light. The results showed under both UV and visible light the order sequence of photocatalytic activity was CT-10 >Evap-10 >Mech-10 (Fig. 7a and b). Mech-10 displayed nearly the same photocatalytic activity as pure {0 0 1}TiO_2, which suggests the absence of a compact connection between g-C_3N_4 and {0 0 1}TiO_2 in the mechanical mixing synthesis. Similarly, the enhanced photocatalytic performance of the CT-10 over the Evap-10 may indicate a closer connection between g-C_3N_4 and {0 0 1}TiO_2 in the g-C_3N_4/{0 0 1}TiO_2 prepared by the solvent-free in situ method in this work.

From data in Fig. 8, it can be calculated that the percentage of {0 0 1} facets in Evap-10 and CT-10 were 36.8% and 58.0%, respectively. The larger percentage of {0 0 1} facets in CT-10 is another reason for its enhanced photocatalytic performance.

The stability of g-C_3N_4/{0 0 1}TiO_2 composite was investigated by performing recycle experiments with CT-10 under visible light irradiation (Fig. 9). After four recycles the photocatalytic activity did not show any obvious decay, demonstrating the high stability of the composite with use. Further, the XRD pattern of CT-10 barely

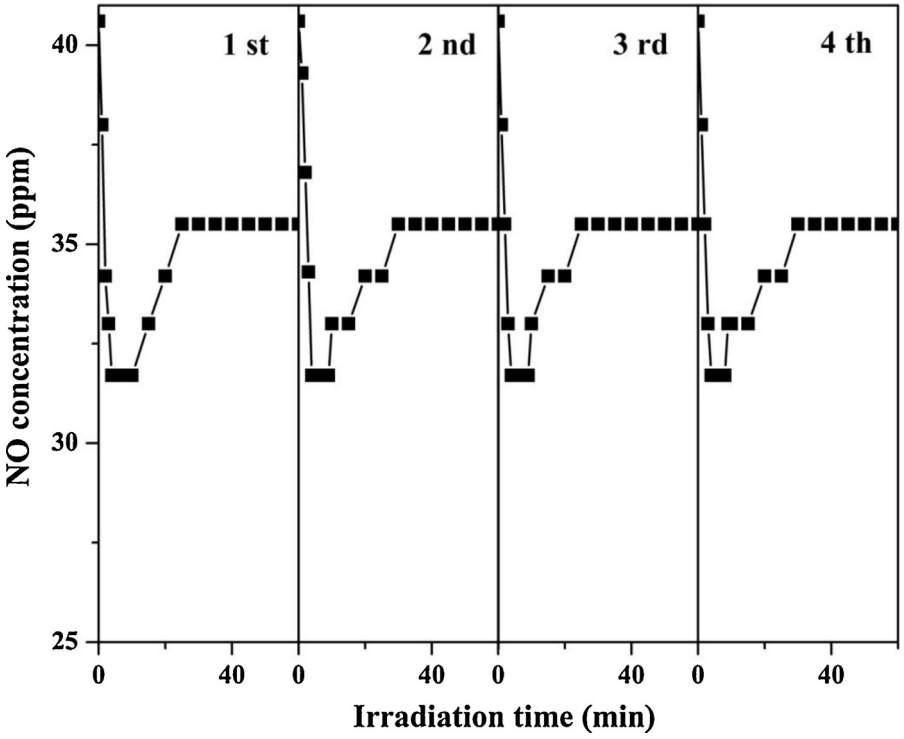

Fig. 9. Recycling experiments with CT-10 under visible light irradiation.

changed after four recycles (Fig. S6), which confirmed the stability of the composite.

3.7. Photoluminescence (PL) and photoelectrochemical analyses

Photoluminescence (PL) analyses are often used to reveal the transfer and separation of photo-generated charge carriers since the PL spectra originate from the recombination of photo-generated electron–hole pairs. The emission peak in Fig. S7 that is centered at ca. 393 nm is attributed to the emission of band gap transition with an energy approximately equal to the band gap energy of anatase {0 0 1}TiO_2 (390 nm) [17]. The peak located around 440 nm is assigned to the recombination of the photo-generated electrons and holes in g-C_3N_4 [52]. The photoluminescence of g-C_3N_4 was clearly inhibited after the g-C_3N_4 was connected with {0 0 1}TiO_2. In other words, the composite with {0 0 1}TiO_2 significantly promotes the separation of photo-generated electron-hole pairs in CT-*x*, which may explain the enhanced photocatalytic activity of CT-*x*.

Photocurrent analyses were conducted for CT-10, Mech-10 and Evap-10 under on-off cyclical visible light irradiation to investigate the interaction between the two components of the g-C_3N_4/{0 0 1}TiO_2 composites prepared by different methods (Fig. 10). A compact connection between the two components in a composite would favor the separation of photo-generated carriers, resulting in a higher photocurrent density. Therefore, the photocurrent density is a reflection of the compactness between the two components. The photocurrent density of Mech-10 electrode was similar to that of {0 0 1}TiO_2, which implied that there was no interaction or an extremely weak interaction between g-C_3N_4 and {0 0 1}TiO_2 in Mech-10. Evap-10 and CT-10 showed a clear increase in photocurrent density compared to pure g-C_3N_4, of which CT-10 exhibited the highest photocurrent density. Under UV light irradiation (Fig. S8), CT-10 also exhibited the highest photocurrent density, which is a confirmation of the stronger interaction between the two components of CT-10, and further implied the importance of compact connection between the two host phases for composite catalyst.

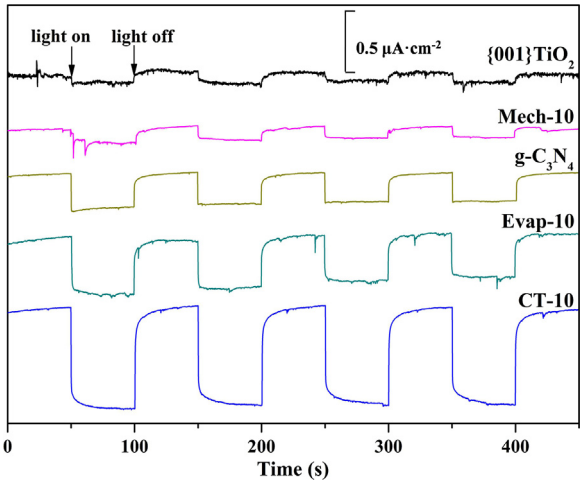

Fig. 10. Photo-generated current densities of g-C_3N_4, {0 0 1}TiO_2, CT-10, Evap-10 and Mech-10 under visible light.

3.8. Proposed synthesis and reaction mechanism

The results above show that a successful construction of g-C_3N_4/{0 0 1}TiO_2 composites was achieved. Based on previous works done by earlier researchers, a possible synthetic route of the composites can be proposed. Specifically, we can imagine that in the synthesis of g-C_3N_4 by urea, gaseous isocyanic acid, cyanic acid, melamine and melem intermediates form at different temperature ranges [46,53,54], which could made our crucible reactor perform like a fluidized bed. The {0 0 1}TiO_2 would be mixed intensively with the reactant in the “fluid bed”. Then, the thermal polycondensation of these gaseous intermediates would take place on the

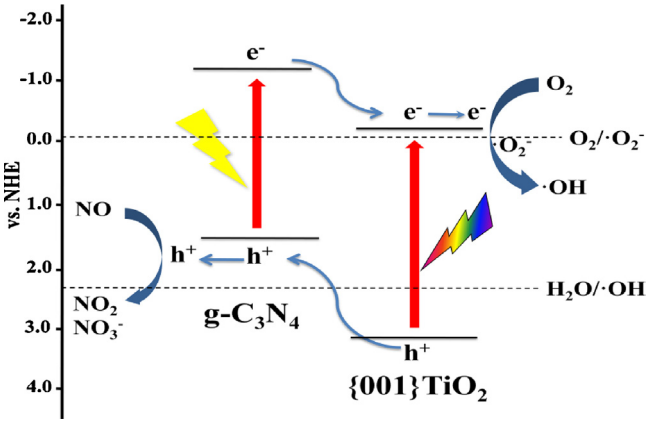

Scheme 1. Proposed photocatalytic reaction mechanisms of g-C_3N_4/{0 0 1}TiO_2 composite under UV and visible light irradiation.

{0 0 1}TiO_2 nanosheets. Finally, a relatively uniform product of g-C_3N_4/{0 0 1}TiO_2 would be obtained (Fig. 3c and d). Simultaneously, F^- ions on {0 0 1}TiO_2(F) would be removed in the calcination process and parts of the {0 0 1} facets would transform into {1 0 1} facets to achieve the balance of surface free energy. However, the growth of g-C_3N_4 on the {0 0 1} facets might help in decreasing its surface free energy. Thus more {0 0 1} facets would be preserved in the presence of g-C_3N_4 (Fig. 1a).

Also, a possible photocatalytic reaction mechanism of g-C_3N_4/{0 0 1}TiO_2 composite can be proposed based on the above analyses. As shown in Scheme 1, when the catalyst was exposed to visible light irradiated, photo-induced electrons were excited from the valence band of g-C_3N_4 with holes remaining in its valence band. These holes could migrate to surface and directly react with contaminants. Electrons in the conduction band of g-C_3N_4 could transport into the conduction band of {0 0 1}TiO_2 due to their conduction band offset. The compact contact between the two materials would further promote this transport process. Electrons on {0 0 1}TiO_2 could react with the adsorbed O_2 and generated superoxide radicals, which is an important reactive oxygen species for contaminants elimination. The photo-generated charge carrier recombination process would be suppressed when the electrons and holes were separated after the electron transport process, resulting in high photocatalytic activity in visible light. On the other hand, in the case of UV light irradiation, not only g-C_3N_4 but also {0 0 1}TiO_2 in the composite could be excited. Then, the photo-generated holes in the valence band of {0 0 1}TiO_2 could transfer into the valence band of g-C_3N_4 due to their valence band offset, whereas the photo-generated electrons would transfer from the conduction band of g-C_3N_4 to that of {0 0 1}TiO_2 due to the conduction band offset. Thus the photo-generated electrons and holes in the composite would be separated sufficiently, resulting in highly effective photocatalytic performance under UV light irradiation.

4. Conclusions

In this work, a simple solvent-free in situ method was used to synthesis a visible light responsive g-C_3N_4/{0 0 1}TiO_2 composite photocatalyst. The results of XRD, FT-IR, XPS, SEM and HRTEM characterizations confirmed the successful synthesis of the g-C_3N_4/{0 0 1}TiO_2 composite and its compact connection between the two components. The XRD results suggest that the growth of g-C_3N_4 during calcinations favors the preservation of the {0 0 1} facets in {0 0 1}TiO_2. The UV–vis DRS results confirmed the visible light responsiveness of composite. In the photo-oxidation of NO, all of the composite samples exhibited higher photocatalytic activity than pure g-C_3N_4 or {0 0 1}TiO_2. The optimal sample of CT-10 was 2.4 times more effective than {0 0 1}TiO_2 under UV light, and 5.8 times more effective than g-C_3N_4 under visible light irradiation, respectively. In addition, the photocatalytic activity and the photocurrent density of CT-10 was significantly higher than that of Mech-10 and Evap-10, indicating that solvent-free in situ synthesis method was a feasible method to obtain high photocatalytic activity composites with compact connected two host phases. The synthesis method reported here is simple and holds the promise of expanded large-scale production and wider use of {0 0 1}TiO_2 based catalysts in the future.

Acknowledgements

This work was supported by National Natural Science Foundation of China (No. 20807015, 21037001, 21277051), Science and Technology Planning Project of Guangzhou City China (No. 12C62081602), and the Fundamental Research Funds for the Central Universities, SCUT (No. 2012ZZ0049). We are grateful for the language help provided by Dr. Donald G. Barnes.

Appendix A. Supplementary data

Supplementary data associated with this article can be found, in the online version, at http://dx.doi.org/10.1016/j.apcatb.2015.10.007.

References

[1] A. Fujishima, K. Honda, Nature 238 (1972) 37–38.
[2] W.J. Zhou, Z.Y. Yin, Y.P. Du, Small 9 (2013) 140–147.
[3] J. Gong, Y. Li, Z. Hu, Z. Zhou, Y. Deng, J. Phys. Chem. C 114 (2010) 9970–9974.
[4] W. Wang, Q. Shang, W. Zheng, H. Yu, X. Feng, Z. Wang, Y. Zhang, G. Li, J. Phys. Chem. C 114 (2010) 13663–13669.
[5] Z. Wu, B. Jiang, Y. Liu, W. Zhao, B. Guan, J. Hazard. Mater. 145 (2007) 488–494.
[6] Y. Hu, X. Song, S.M. Jiang, C.H. Wei, Chem. Eng. J. 274 (2015) 102–112.
[7] M. Pelaez, N.T. Nolan, S.C. Pillai, M.K. Seery, P. Falaras, A.G. Kontos, P.S.M. Dunlop, J.W.J. Hamilton, J.A. Byrne, K. O'Shea, M.H. Entezari, D.D. Dionysiou, Appl. Catal. B: Environ. 125 (2012) 331–349.
[8] J.W. Tang, Z.G. Zou, J.H. Ye, Catal. Lett. 92 (2004) 53–56.
[9] C. Hefeng, H. Baibiao, D. Ying, Nanoscale 6 (2014) 2009–2026.
[10] R. Hu, X. Xiao, S. Tu, X. Zuo, J. Nan, Appl. Catal. B: Environ. 163 (2015) 510–519.
[11] U.M. Garcia-Perez, A. Martinez-de La Cruz, J. Peral, Electrochim. Acta 81 (2012) 227–232.
[12] I.M. Szilagyi, B. Forizs, O. Rosseler, A. Szegedi, P. Nemeth, P. Kiraly, G. Tarkanyi, B. Vajna, K. Varga-Josepovits, K. Laszlo, A.L. Toth, P. Baranyai, M. Leskela, J. Catal. 294 (2012) 119–127.
[13] S. Rengaraj, S. Venkataraj, C. Tai, Y. Kim, E. Repo, M. Sillanpaa, Langmuir 27 (2011) 5534–5541.
[14] Z. Li, P. Zhang, T. Shao, X. Li, Appl. Catal. B: Environ. 125 (2012) 350–357.
[15] S. Yin, B. Liu, P. Zhang, T. Morikawa, K. Yamanaka, T. Sato, J. Phys. Chem. C 112 (2008) 12425–12431.
[16] C. Chen, W. Ma, J. Zhao, Chem. Soc. Rev. 39 (2010) 4206–4219.
[17] Q. Xiang, J. Yu, M. Jaroniec, Nanoscale 3 (2011) 3670–3678.
[18] M. Liu, L. Piao, W. Lu, S. Ju, L. Zhao, C. Zhou, H. Li, W. Wang, Nanoscale 2 (2010) 1115–1117.
[19] G. Liu, H.G. Yang, X. Wang, L. Cheng, J. Pan, G.Q.M. Lu, H. Cheng, J. Am. Chem. Soc. 131 (2009) 12868.
[20] J. Yu, G. Dai, Q. Xiang, M. Jaroniec, J. Mater. Chem. 21 (2011) 1049–1057.
[21] Q. Xiang, J. Yu, M. Jaroniec, Phys. Chem. Chem. Phys. 13 (2011) 4853–4861.
[22] K. Nagaveni, M.S. Hegde, G. Madras, J. Phys. Chem. B 108 (2004) 20204–20212.
[23] F. Quan, Y. Hu, X. Zhang, C. Wei, Appl. Surf. Sci. 320 (2014) 120–127.
[24] J. Yu, L. Qi, M. Jaroniec, J. Phys. Chem. C 114 (2010) 13118–13125.
[25] S. Zhu, S. Liang, Q. Gu, L. Xie, J. Wang, Z. Ding, P. Liu, Appl. Catal. B: Environ. 119 (2012) 146–155.
[26] Q.C. Xu, D.V. Wellia, Y.H. Ng, R. Amal, T.T.Y. Tan, J. Phys. Chem. C 115 (2011) 7419–7428.
[27] X. Wang, K. Maeda, A. Thomas, K. Takanabe, G. Xin, J.M. Carlsson, K. Domen, M. Antonietti, Nat. Mater. 8 (2009) 76–80.
[28] Y. Wang, R. Shi, J. Lin, Y. Zhu, Energy Environ. Sci. 4 (2011) 2922–2929.
[29] Daimei Chen, Kewei Wang, Dugao Xiang, Ruilong Zong, Wenqing Yao, Yongfa Zhu, Appl. Catal. B: Environ. 147 (2014) 554–561.
[30] Daimei Chen, Kewei Wang, Wangzhi Hong, Ruilong Zong, Wenqing Yao, Yongfa Zhu, Appl. Catal. B: Environ. 166–167 (2015) 366–373.
[31] Ze'ai Huang, Qiong Sun, Kangle Lv, Zehui Zhang, Mei Li, Bing Li, Appl. Catal. B: Environ. 164 (2015) 420–427.
[32] L. Gu, J. Wang, Z. Zou, X. Han, J. Hazard. Mater. 268 (2014) 216–223.

[33] K. Dai, L. Lu, C. Liang, Q. Liu, G. Zhu, Appl. Catal. B: Environ. 156 (2014) 331–340.
[34] A. Selloni, Nat. Mater. 7 (2008) 613–615.
[35] M. Jung, M. Chu, M.G. Kang, Chem. Commun. 48 (2012) 5016–5018.
[36] J.S. Jang, E.S. Kim, S.H. Choi, D.H. Kim, H.G. Kim, J.S. Lee, Appl. Catal. A: Gen. 427–428 (2012) 106–113.
[37] G. Guo, Y. Hu, S. Jiang, C. Wei, J. Hazard. Mater. 223 (2012) 39–45.
[38] M. Sofianou, V. Psycharis, N. Boukos, T. Vaimakis, J. Yu, R. Dillert, D. Bahnemann, C. Trapalis, Appl. Catal. B: Environ. 142 (2013) 761–768.
[39] S. Zhou, Y. Liu, J. Li, Y. Wang, G. Jiang, Z. Zhao, D. Wang, A. Duan, J. Liu, Y. Wei, Appl. Catal. B: Environ. 158 (2014) 20–29.
[40] J. Sun, Y. Yuan, L. Qiu, X. Jiang, A. Xie, Y. Shen, J. Zhu, Dalton Trans. 41 (2012) 6756–6763.
[41] G. Liao, S. Chen, X. Quan, H. Yu, H. Zhao, J. Mater. Chem. 22 (2012) 2721–2726.
[42] G. Zhang, J. Zhang, M. Zhang, X. Wang, J. Mater. Chem. 22 (2012) 8083–8091.
[43] C. Miranda, H. Mansilla, J. Yanez, S. Obregon, G. Colon, J Photochem. Photobiol. A 253 (2013) 16–21.
[44] J.M. Ruso, V. Verdinelli, N. Hassan, O. Pieroni, P.V. Messina, Langmuir 29 (2013) 2350–2358.
[45] Y. Cao, Z. Zhang, J. Long, J. Liang, H. Lin, H. Lin, X. Wang, J. Mater. Chem. A 2 (2014) 17797–17807.
[46] X. Zou, G. Li, Y. Wang, J. Zhao, C. Yan, M. Guo, L. Li, J. Chen, Chem. Commun. 47 (2011) 1066–1068.
[47] H. Li, J. Liu, W. Hou, N. Du, R. Zhang, X. Tao, Appl. Catal. B: Environ. 160 (2014) 89–97.
[48] Z. Sheng, L. Shao, J. Chen, W. Bao, F. Wang, X. Xia, ACS Nano 5 (2011) 4350–4358.
[49] H. Zhao, H. Yu, X. Quan, S. Chen, H. Zhao, H. Wang, RSC Adv. 4 (2014) 624–628.
[50] Y. Chen, W. Huang, D. He, S. Yue, H. Huang, ACS Appl. Mater. Inter. 6 (2014) 14405–14414.
[51] P. Niu, L. Zhang, G. Liu, H. Cheng, Adv. Funct. Mater. 22 (2012) 4763–4770.
[52] F. Dong, Z. Zhao, T. Xiong, Z. Ni, W. Zhang, Y. Sun, W. Ho, ACS Appl. Mater. Inter. 5 (2013) 11392–11401.
[53] B. Jurgens, E. Irran, J. Senker, P. Kroll, H. Muller, W. Schnick, J. Am. Chem. Soc. 125 (2003) 10288–10300.
[54] A. Thomas, A. Fischer, F. Goettmann, M. Antonietti, J. Mueller, R. Schloegl, J.M. Carlsson, J. Mater. Chem. 18 (2008) 4893–4908.